JOURNAL OF AIRCRAFT
Vol. 32, No. 4, July–August 1995

Drag Prediction at Subsonic and Transonic Speeds Using Euler Methods

C. P. van Dam,* K. Nikfetrat,† and K. Wong‡
University of California, Davis, Davis, California 95616
and
P. M. H. W. Vijgen§
High Technology Corporation, Hampton, Virginia 23666

A technique for the evaluation of aerodynamic drag from flowfield solutions based on Euler equations is discussed. The technique is based on the application of the momentum theorem to a control surface enclosing the configuration and it allows the decomposition of the total drag into induced drag and wave drag. Consequently, it provides more physical insight into the drag sources than the conventional surface-pressure integration technique. The induced drag is obtained from the integration of the kinetic energy of the trailing vortex system on a wake plane and the wave drag is obtained from the integration of the entropy jump over the shocks. The drag-evaluation technique is applied to three-dimensional steady flowfield solutions for the ONERA M6 wing as well as an AR-7 wing with an elliptic spanwise chord distribution and a NACA 0012 section shape. Comparisons between the drag obtained with the present technique and the drag based on the integration of surface pressures are presented for several Euler codes.

Introduction

THE aerodynamic drag of an aircraft flying at subsonic speeds can be separated into the viscous drag and the induced (or vortex) drag. The former is generated through the action of the viscosity in the boundary layer, whereas the latter is the result of the shedding of vorticity that accompanies the production of lift. Here, we limit ourselves to inviscid attached flows and, consequently, the only drag component is the induced drag. At transonic and supersonic speeds another drag-producing mechanism arises from the radiation of energy away from the aircraft in the form of pressure waves; i.e., the wave drag.

The total inviscid drag can be determined by integrating the pressure acting on the surface of the aircraft. This so-called near-field technique can lead to inaccuracies in the drag calculation because it involves the near cancellation of a large force component in the thrust direction and a slightly larger force component in the drag direction.[1] Also, this technique does not allow the separation of the drag into its two physical components: 1) induced drag and 2) wave drag. This drag breakdown capability is especially important in the design phase when the performance characteristics of the aircraft are being maximized by refining and improving its shape. The efficiency of this design process can be greatly enhanced when the physical mechanisms, whereby the drag is created, can be identified. For this reason, far-field techniques based on the integration of the momentum flux along a closed contour enclosing the configuration have been applied to evaluate the drag and its components. These far-field techniques have been shown to be very useful and accurate in the evaluation of potential-flow solutions at subsonic and transonic conditions.[2] However, a fundamental difference exists in the application of the field integral to solutions based on the potential-flow equations and on the Euler equations.[2,3] The latter formulation of the governing equations is preferred because it can provide a more accurate modeling of the vortical field in the flow and it is not limited to flows with weak shocks. Hence, the theory presented in this article is developed for Euler solutions.

In previous papers,[4,5] the technique based on the integration of the surface pressure and two far-field techniques (one based on the integration of the momentum flux along a contour enclosing the configuration and the second based on the evaluation of a wake integral), are described and applied to three-dimensional Euler solutions for wings with attached flow at low Mach number conditions. These results demonstrate that the far-field technique based on the wake integral provides the most consistent and accurate induced-drag predictions. Both the surface pressure integration technique and the momentum integration technique tend to give erroneous drag values, mainly as a result of the inherent numerical viscosity in the Euler solutions.

The purpose of this article is to extend the formulation for the prediction of induced drag described in Refs. 4 and 5 to compressible flow conditions and to include a separate prediction technique for wave drag. In the following section, a detailed discussion is presented on the evaluation of the aerodynamic force on lifting and nonlifting configurations. Next, the technique is applied to determine the drag from Euler solutions for two wing configurations at subsonic and transonic conditions.

Force-Evaluation Methodology

The far-field expression for the aerodynamic force on a configuration in an unbounded uniform flow $v = iU_\infty$ can be obtained by integrating the pressure and momentum flux over the far surface S_{far} of a closed control volume enclosing the configuration:

$$F_b = -\int_{S_{far}} [pn + \rho v(v\cdot n)]\, dS \qquad (1)$$

Received May 1, 1993; revision received May 3, 1994; accepted for publication Feb. 21, 1995.

*Professor, Department of Mechanical and Aeronautical Engineering. Senior Member AIAA.

†Ph.D. Candidate; currently Postdoctoral Researcher, Department of Mechanical Engineering, University of Victoria, Victoria, Canada.

‡Post Graduate Researcher. Member AIAA.

§Research Scientist; currently Senior Specialist Engineer, HSCT Aerodynamics, Boeing Commercial Airplane Group, Seattle, WA 98129. Senior Member AIAA.

where p is the static pressure, ρ is the density, $v = iu + jv + kw$ is the flow velocity, and n is the unit outward normal to the control volume. By moving the inlet plane S_1 far upstream of the body, such that all flow perturbations on it vanish and by letting S_1 and the exit plane S_2 become of infinite radius, where these two planes are normal to the freestream, the i component (drag D) and the k component (lift L) of Eq. (1) become

$$D = -\int_{S_2} [(p + \rho u^2) - (p + \rho u^2)_\infty] \, dS \tag{2}$$

$$L = -\int_{S_2} (\rho u w) \, dS \tag{3}$$

It should be noted that these expressions for the lift and the drag are also valid in viscous flows as long as S_2 is located far enough downstream from the configuration (on the order of one chord length) so that the viscous stresses in the wake are negligible. Equations (2) and (3) can be expressed in terms of gradients of the flow variables on the exit plane S_2. Introducing the position vector $r = jy + kz$ and noting that for $M_\infty < 1$ all flow variables approach their freestream values at the edge of the infinite plane, it can be shown that

$$D = \frac{1}{2} \int_{S_2} [(r \cdot \nabla)(p + \rho u^2)] \, dS \tag{4}$$

In this gradient form it is possible to decompose the total drag into the various drag sources.

The crossflow velocity components v and w and the magnitude of the velocity vector $q^2 = v \cdot v$ are used to isolate the induced drag. Also, the first and second laws of thermodynamics are combined to obtain

$$\nabla p = \rho \nabla h - \rho T \nabla s \tag{5}$$

and to isolate the wave drag where h is enthalpy, T is the temperature, and s is the entropy. Hence, the expression (4) for the drag (without any approximation) becomes

$$D = \frac{1}{2} \int_{S_2} \left\{ r \cdot \left[\rho \nabla \left(h + \frac{1}{2} q^2 \right) - \rho T \nabla s - \frac{1}{2} \rho \nabla (v^2 + w^2) + \frac{1}{2} \rho \nabla u^2 + u^2 \nabla \rho \right] \right\} dS \tag{6}$$

Since the total enthalpy $H = h + \frac{1}{2} q^2$ remains constant in the absence of external work or heat addition, the first term in the integral in Eq. (6) vanishes. The second term in Eq. (6) is the entropy term and it can be expanded as follows:

$$\begin{aligned} \text{Term II} &= -1/(2R) \int_{S_2} [p(r \cdot \nabla)s] \, dS \\ &= -p_\infty/(2R) \int_{S_2} [(r \cdot \nabla)s] \, dS \\ &\quad - 1/(2R) \int_{S_2} [\Delta p (r \cdot \nabla)s] \, dS \end{aligned} \tag{7}$$

where $\Delta p = p - p_\infty$ and R is the gas constant. It can be shown that Eq. (7) can be rewritten in the following form:

$$\text{Term II} = p_\infty/R \int_{S_2} \Delta s \, dS - 1/(2R) \int_{S_2} [\Delta p (r \cdot \nabla)s] \, dS \tag{8}$$

where $\Delta s = s - s_\infty$. For S_2 at $x \to \infty$ and zero-lift conditions, the pressure perturbation Δp and, hence, the contribution of the second integral in Eq. (8) vanishes. The first integral in Eq. (8) represents the expression commonly used for calculating the wave drag D_w (see Refs. 6–9 for wave-drag expressions that are very similar or identical in form, but are deduced differently). For lifting conditions Δp remains finite, even for S_2 at $x \to \infty$, and the second term represents a very small interaction drag (Ref. 9). Since the entropy is conserved everywhere, except at the shocks, the first integral in Eq. (8) may be evaluated across the shocks instead of over the plane S_2 far downstream of the configuration.

The third term in Eq. (6) represents the crossflow kinetic energy and it can be expanded as follows:

$$\begin{aligned} \text{Term III} &= -\frac{1}{4} \int_{S_2} \{r \cdot [\rho \nabla (v^2 + w^2)]\} \, dS \\ &= \frac{1}{2} \int_{S_2} [\rho (v^2 + w^2)] \, dS \\ &\quad + \frac{1}{4} \int_{S_2} [(v^2 + w^2)(r \cdot \nabla)\rho] \, dS \end{aligned} \tag{9}$$

Before proceeding further with the analysis of Eq. (9) it is helpful to inspect the remaining terms in Eq. (6) (Terms IV and V) more closely. These terms can be rearranged in the following form:

$$\begin{aligned} \text{Terms IV + V} &= \frac{1}{4} \int_{S_2} [(r \cdot \nabla)(\rho u^2)] \, dS \\ &\quad + \frac{1}{4} \int_{S_2} [u^2 (r \cdot \nabla)\rho] \, dS \end{aligned} \tag{10}$$

By using conservation of mass and introducing the perturbation velocity in the freestream direction $\Delta u = u - U_\infty$, Eqs. (9) and (10) can be expanded in

$$\begin{aligned} \text{Terms III + IV + V} &= \frac{1}{2} \int_{S_2} [\rho (v^2 + w^2)] \, dS \\ &\quad - \frac{1}{2} \int_{S_2} (\rho \Delta u^2) \, dS + U_\infty/2 \int_{S_2} [\Delta u (r \cdot \nabla)\rho] \, dS \\ &\quad + \frac{1}{4} \int_{S_2} [(v^2 + w^2 + \Delta u^2)(r \cdot \nabla)\rho] \, dS \end{aligned} \tag{11}$$

For subcritical flows the perturbation velocity Δu is solely due to the acceleration of the flow in the cores of the trailing vortex system, whereas for supercritical flows Δu contains also a contribution from the jump in the velocity across the shock waves. Using the approach developed in Ref. 5, the first integral in Eq. (11) can be expressed as

$$\begin{aligned} &\frac{1}{2} \int_{S_2} [\rho (v^2 + w^2)] \, dS \\ &\quad = \frac{1}{2} \int_{S_2} \left\{ \psi \left[\frac{\partial (\rho w)}{\partial y} - \frac{\partial (\rho v)}{\partial z} \right] - \phi g \right\} dS \end{aligned} \tag{12}$$

where $\phi(y, z)$ and $\psi(y, z)$ represent the crossflow potential and stream function, respectively, and $g = -1/\rho \, \partial(\rho u)/\partial x$. If S_2 is far downstream of the configuration then the flow becomes essentially two dimensional and the density variation becomes negligible. Also, the perturbation in the freestream component of the velocity is small compared to the contribution of the crossflow velocity components (e.g., Ref. 10). Consequently, Eq. (11) simplifies to

$$\text{Terms III + IV + V} = \rho_\infty/2 \int_{S_2} (\psi \xi) \, dS \tag{13}$$

where ξ represents the vorticity components in the freestream direction. This integral represents the expression commonly used for calculating the induced drag D_i and it only has to be evaluated over the small region in S_2 that contains trailing vorticity. It is important to note that since the flow is circulation preserving, the integral in Eq. (13) may be evaluated immediately downstream of the configuration.

To a close approximation the expression (6) for the drag can now be written as

$$D = D_w + D_i = p_\infty/R \int_{S_{2,w}} \Delta s \, dS + \rho_\infty/2 \int_{S_{2,i}} (\psi\xi) \, dS \tag{14}$$

This expression is applied to evaluate the total drag and its components from numerical solutions of the Euler equations for subsonic and transonic flows past lifting and nonlifting configurations. The wave drag is obtained from the jump in entropy across the shock system. This calculation should be conducted just downstream of the shocks, but ahead of the trailing edge to avoid capturing any spurious entropy associated with the vortical wake development. However, the latter requirement can often not be met for swept-wing configurations. To get around this problem for swept configurations with swept shocks, the sectional wave drag is calculated by evaluating the entropy jump for each span station. Next, the total wave drag is approximated by integration of the sectional contributions over the entire span of the configuration.

The expansion of the expression for the lift [Eq. (3)] is discussed in Ref. 5. The application of Stokes' theorem allows us to write Eq. (3) in the cross-product form

$$L = \int_{S_2} \{y[\nabla \times (\rho uv)] \cdot i\} \, dS \tag{15}$$

or, by observing that the perturbation in the freestream component of the velocity is small compared to U_∞

$$L = U_\infty \int_{S_2} \left\{ y \left[\frac{\partial(\rho w)}{\partial y} - \frac{\partial(\rho v)}{\partial z} \right] \right\} dS \tag{16}$$

Again, for S_2 at $x \to \infty$ the variation in the density can be neglected and

$$L = \rho_\infty U_\infty \int_{S_2} (y\xi) \, dS \tag{17}$$

It is of some interest to note that the integral in Eq. (17) only has to be evaluated over the region that contains vorticity, and, because the flow is circulation preserving, may be evaluated immediately downstream of the configuration.

Euler Codes

The codes used in the present study to generate the flowfield solutions are referred to as TLNS3D, LANS3D, and CFL3D.

TLNS3D is a cell-centered finite volume method with a long history going back to Jameson et al.[11] and more recently further developed by Vatsa and his co-workers (e.g., Ref. 12). It uses an explicit five-stage Runge-Kutta time-marching algorithm with second-order central differences for the spatial derivatives. Second- and fourth-order dissipation terms are added for numerical stability. Convergence is accelerated through utilization of the multigrid technique as well as implicit residual smoothing.

LANS3D is a finite difference method developed by Obayashi, Fujii, and co-workers (Refs. 13 and 14). The governing equations are integrated numerically in time by the lower/upper-alternating direction implicit (LU-ADI) factorization algorithm until a steady-state solution is obtained. This algorithm provides a compromise between the LU and ADI algorithms in which each ADI operator is decomposed into the product of lower and upper bidiagonal matrices by a flux-vector-splitting technique and a diagonally dominant factorization. Both second- and fourth-order dissipation terms are added for numerical stability.

CFL3D is a cell-centered finite volume method developed by Thomas, Anderson, and others (Refs. 15 and 16). It uses the ADI time-marching algorithm with third-order upwind-biased differences for the spatial derivatives. The upwind method used is the Roe flux-difference splitting, whereas the min-mod flux limiting scheme is used to obtain smooth solutions in the vicinity of discontinuities. Here the multigrid option (V-cycle) is employed to accelerate the convergence rate.

Test Cases

The test cases used for evaluation of the drag characteristics are the $X_t = 1.0$ wing and the ONERA M6 wing.

The $X_t = 1.0$ wing was developed for induced-drag studies and is described in Ref. 17. The pertinent points of this wing configuration are its unswept straight trailing edge and curved leading edge (Fig. 1). It has an elliptic spanwise chord distribution, a root chord $c_r = 1.0$ (reference length), a semispan $b/2 = 2.749$, and an AR $= 7.0$. The elliptic spanwise chord distribution results in a chord length of zero at the tip. To avoid numerical difficulties in this region the wing is given a small but finite chord length at the tip $c_t \approx 0.05$ by terminating the span at $\eta = y/(b/2) = 0.999$. The sectional shape is provided by the sharp trailing-edge version of the NACA 0012 airfoil.

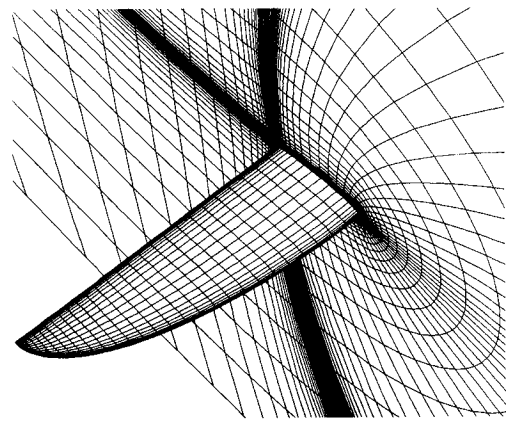

Fig. 1 Surface grid representation of the $X_t = 1.0$ wing.

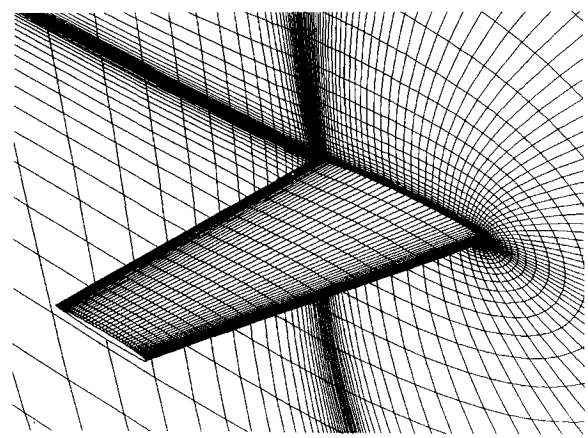

Fig. 2 Surface grid representation of the ONERA M6 wing.

The ONERA M6 wing was developed to provide a test case for code validation at subsonic and transonic speeds and a large volume of experimental and computational data are available for this configuration.[18,19] The wing is modeled such that the root chord $c_r = 1.0$ (reference length), the tip chord $c_t = 0.563$, the semispan $b/2 = 1.476$, and the AR = 3.8 (Fig. 2). The leading edge has a constant sweep angle of 30 deg and the sectional shape in the freestream direction is provided by the airfoil coordinates from Table 7-5 in Ref. 19. Presently, the postanalysis procedure to evaluate the drag is limited to flowfield solutions on C-H grids. Consequently, the actual rounded tip geometry tested in the experiment is not modeled.

Results and Discussion

Most of the results presented and discussed in this article are based on flowfield solutions obtained using TLNS3D with the second- and fourth-order dissipation terms reduced to minimum values for numerical stability and the residual error reduced at least five orders of magnitude. The results based on flowfield solutions obtained using LANS3D and CFL3D are taken from Ref. 20. The TLNS3D and LANS3D solutions were obtained on the Cray Y-MP (Eagle) of the NASA Ames Research Center. Due to the in-core limitation of 12 MWords of this computer, the grids typically consist of 250,000 points with the far-field boundaries at 6–8 reference lengths away from the wing surface. Special attention is paid to the grid spacing near the leading and trailing edges of the wings as well as the tips (see Figs. 1 and 2). At the leading edges and the trailing edges the chordwise grid spacing (nondimensionalized with reference to reference length) is reduced to 0.001 and 0.0001, respectively, and at the tips the spanwise grid spacing (nondimensionalized with respect to semispan) is reduced to less than 0.01.

In Figs. 3–5 and Table 1 the results for the $X_t = 1.0$ wing at an angle of attack $\alpha = 4$ deg and freestream Mach number $M_\infty = 0.20$ are presented. The upper surface pressure contours (Fig. 3) depict a well-behaved two-dimensional flow pattern for most of the wing. The spanwise load distribution (Fig. 4) matches the classic elliptic distribution well and this

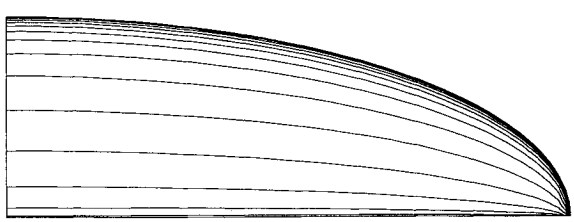

Fig. 3 Upper surface pressure contours for $X_t = 1.0$ wing at $M_\infty = 0.20$ and $\alpha = 4$ deg (TLNS3D).

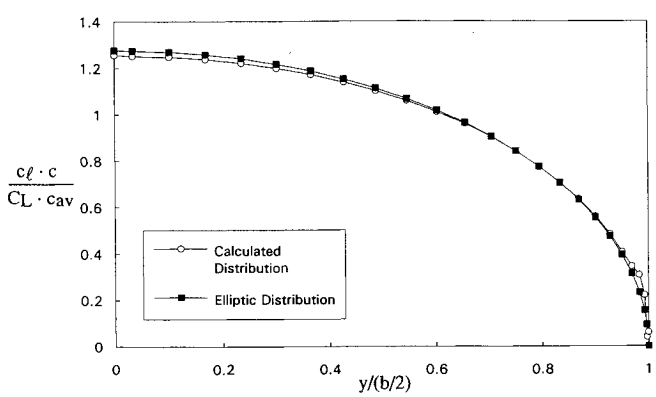

Fig. 4 Spanwise loading distribution for $X_t = 1.0$ wing at $M_\infty = 0.20$ and $\alpha = 4$ deg (TLNS3D). Here, c_l is the sectional lift coefficient, c is the local chord, and $c_{av} = S/b$ is the average chord.

Table 1 Lift and drag coefficients as obtained from surface pressure integration and wake evaluating technique for $X_t = 1.0$ wing at $\alpha = 4$ deg and $M_\infty = 0.20$ (TLNS3D)

	C_L	C_D
Surface pressure integration	0.3426	0.0063
Wake analysis technique	0.3425	0.0054 (induced)
Linear theory ($C_L = 0.3425$)	——	0.0053

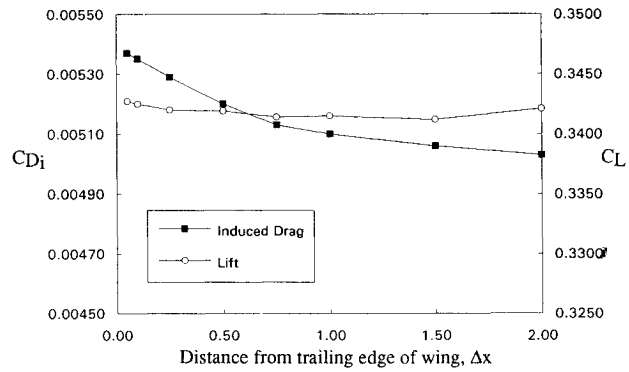

Fig. 5 Variation in computed lift coefficient C_L and induced-drag coefficient C_{D_i} with streamwise location of integration plane for $X_t = 1.0$ wing at $M_\infty = 0.20$ and $\alpha = 4$ deg (TLNS3D).

serves as a benchmark against which the accuracy of the predicted drag values are assessed. The predicted values for the lift coefficient $C_L = 2L/(\rho_\infty U_\infty^2 S)$ and the drag coefficient $C_D = 2D/(\rho_\infty U_\infty^2 S)$ are presented in Table 1. The trailing vorticity distribution is evaluated just downstream of the wing at $\Delta x = 0.1$, and from the results of Table 1 it is clear that there is excellent agreement between the lift coefficient obtained from the evaluation of the wake integral [Eq. (17)] and the lift coefficient obtained from the integration of surface pressures. This provides a check on the consistency of the numerical solution as well as the drag prediction. Previous reported results obtained with LANS3D and CFL3D give values for the lift coefficient within 2% of the present $C_L = 0.3426$.[5,20] According to linear theory the (induced) drag and the lift for a wing with an elliptic spanwise loading are related as follows: $C_D = C_L^2/(\pi\ \mathrm{AR})$. For high-AR unswept wings at incompressible conditions this expression for the drag is known to be quite accurate. The results in Table 1, however, indicate that the drag obtained from surface-pressure integration differs by more than 10 counts from the linear-theory value, whereas the drag obtained from the wake integral [Eq. (13)] is within 1 count. Similar discrepancies in the drag values based on surface-pressure integration using LANS3D and CFL3D are reported elsewhere.[5,20] In the section describing the force-evaluation methodology it was argued that lift as well as induced drag may be computed by evaluating the respective integrals for any downstream location of the wake plane S_2. The question arises as to whether this result may be realized in these numerical solutions of the Euler equations. In Fig. 5 the computed lift coefficient and induced-drag coefficient are plotted for a range of wake-plane locations. The computed values at $\Delta x = 0.1$ are those listed in Table 1. The lift coefficient is shown to vary by about 0.001, whereas the drag coefficient gradually diminishes by 3.5 counts from 0.00538 just downstream of the wing to 0.00502 at $\Delta x = 2.0$. The loss in accuracy of the computed forces with increasing distance from the trailing edge is the result of the rapidly expanding grid spacing in the streamwise direction (see Fig. 1).

The next two cases deal with transonic nonlifting flows. In Fig. 6 the surface pressure contours are depicted for the $X_t = 1.0$ wing at zero angle of attack and $M_\infty = 0.85$. The predicted values for the force coefficients are presented in Table 2. This test case serves to check the prediction technique

Table 2 Lift and drag coefficients as obtained from surface pressure integration and wake evaluating technique for X_t = 1.0 wing at α = 0 deg and M_∞ = 0.85 (LANS3D)

	C_L	C_D
Surface pressure integration	0.0000	0.0196
Wake analysis technique	0.0000	0.0000 (induced)
		0.0193 (wave)
		0.0193 (total)

Table 3 Lift and drag coefficients as obtained from surface pressure integration and wake evaluating technique for ONERA M6 wing at α = 0 deg and M_∞ = 0.92 (TLNS3D)

	C_L	C_D
Surface pressure integration	0.0000	0.0230
Wake analysis technique	0.0000	0.0000 (induced)
		0.0219 (wave)
		0.0219 (total)

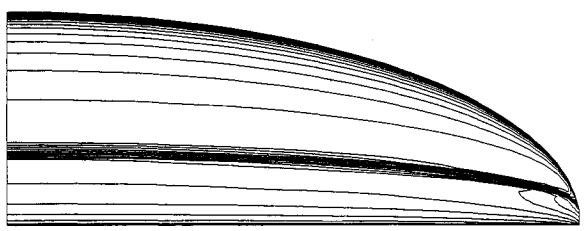

Fig. 6 Surface pressure contours for X_t = 1.0 wing at M_∞ = 0.85 and α = 0 deg (LANS3D).

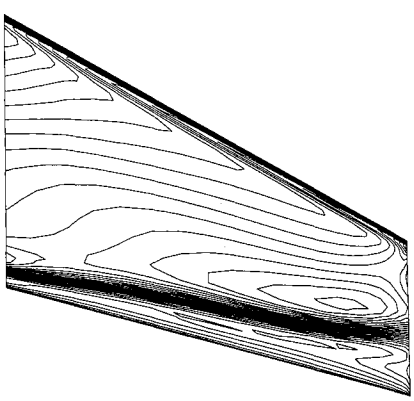

Fig. 7 Upper surface pressure contours for ONERA M6 wing at M_∞ = 0.92 and α = 0 deg (TLNS3D).

for the wave drag because there is no lift and, therefore, no induced drag. The pressure contours in Fig. 6 clearly depict the shock development. The wave drag obtained by evaluating the entropy rise across the shocks agrees well with the drag obtained by integrating surface pressure, indicating that the evaluation of wave drag from three-dimensional Euler solutions can be performed with acceptable accuracy.

In Fig. 7 and Table 3 the results from the ONERA M6 wing at zero angle of attack and M_∞ = 0.92 are presented. The surface pressure contours depicted in Fig. 7 are very similar to those reported in Ref. 16 for this test case. Also, the values of the wave drag listed in Table 3 fall within the range of values reported in Ref. 16, and again, the value obtained by evaluating the entropy rise across the shocks is in fair agreement with the value obtained by integrating surface pressure.

We have shown that Eqs. (13) and (17) are valid to evaluate the induced drag and lift, respectively, and that Eq. (8) can

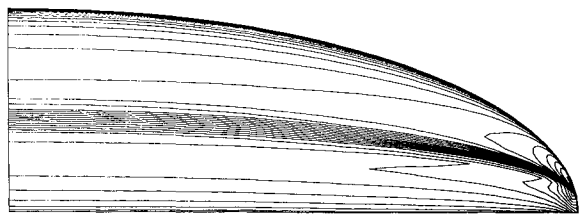

Fig. 8 Upper surface pressure contours for X_t = 1.0 wing at M_∞ = 0.78 and α = 4 deg (TLNS3D).

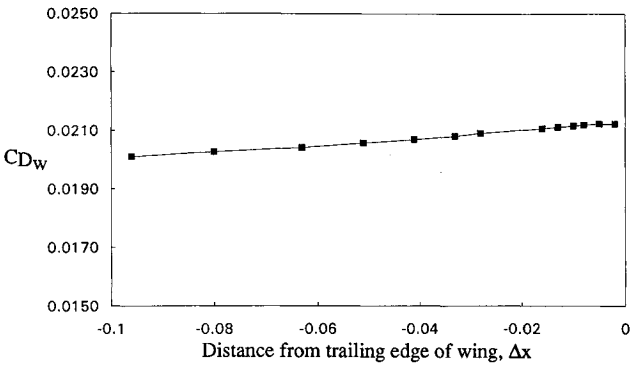

Fig. 9 Variation in computed wave-drag coefficient C_{D_w} with streamwise location of integration plane ahead of trailing edge for X_t = 1.0 wing at M_∞ = 0.78 and α = 4 deg (TLNS3D).

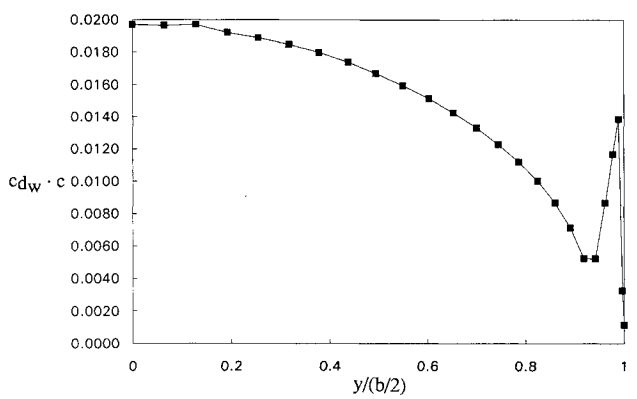

Fig. 10 Spanwise wave-drag distribution for X_t = 1.0 wing at M_∞ = 0.78 and α = 4 deg (TLNS3D). Here, c_{d_w} is the sectional wave-drag coefficient and c is the local chord.

be used to evaluate the wave drag at nonlifting conditions. The next two cases will indicate if the present drag evaluation technique can be used to decompose the total inviscid drag of a lifting wing at transonic flow conditions with acceptable accuracy into induced drag and wave drag. In Figs. 8–10 and Table 4 the results for the X_t = 1.0 wing at α = 4 deg and M_∞ = 0.78 are presented. The surface pressure contours in Fig. 8 depict the strong shock on the wing upper surface. The predicted lift coefficients are in good agreement, demonstrating that the wake-analysis technique also works well at these transonic lifting conditions. In Table 4 the sum of the wave drag and the induced drag is also listed and shown to be in excellent agreement with the drag value obtained from integration of the surface pressures. Also, the question arises in what manner the wave drag as computed from the numerical solutions of the Euler equations is affected by the streamwise location of the integration plane. In Fig. 9 the wave drag as computed from the wake integral is shown for a range of wake-plane locations. The wave-drag value computed at $\Delta x = -0.1$ is listed in Table 4. The results demonstrate that the computed value for the wave-drag coefficient increases gradually with increasing distance from the shock.

Table 4 Lift and drag coefficients as obtained from surface pressure integration and wake evaluating technique for $X_t = 1.0$ wing at $\alpha = 4$ deg and $M_\infty = 0.78$ (TLNS3D)

	C_L	C_D
Surface pressure integration	0.4803	0.0304
Wake analysis technique	0.4842	0.0104 (induced)
		0.0200 (wave)
		0.0304 (total)

Table 5 Lift and drag coefficients as obtained from surface pressure integration and wake evaluating technique for $X_t = 1.0$ wing at $\alpha = 4$ deg and $M_\infty = 0.80$ (CFL3D)

	C_L	C_D
Surface pressure integration	0.5265	0.0421
Wake analysis technique	0.5353	0.0127 (induced)
		0.0290 (wave)
		0.0417 (total)

Spurious entropy production in the region of the flowfield downstream of the shock causes this increase in the computed drag.

The virtue of the present prediction technique based on the wake analysis as a configuration analysis tool is further exemplified by the results in Fig. 10. In this figure the spanwise distribution of the wave drag as obtained from the evaluation of the wave-drag integral is depicted. The results show that most of the wave drag is generated in the root region of the wing; not surprising given the zero sweep angle at the wing root. More surprising is the spike in the wave-drag distribution in the wingtip region. Under the influence of the trailing-vortex system the downwash angles are smaller and, consequently, the sectional lift coefficients are higher in this region. This causes an increase in the shock strength and the rapid rise in the sectional wave-drag coefficient near the wingtip. The drag breakdown in Table 4 indicates that the wave drag provides about 65% of the total inviscid drag and that the induced drag is near its minimal value for the given wing AR and lift coefficient. The above information enables us to conclude that the inviscid performance characteristics of the present configuration at the given conditions can mainly be improved by modifying the wing shape to reduce the shock strength and, thus, the wave drag. This decision is not clear-cut when one has only the drag information based on the surface pressure integration.

For completeness, the results for the $X_t = 1.0$ wing at $\alpha = 4$ deg and $M_\infty = 0.80$ are summarized in Table 5. A comparison with the data in Table 4 shows that the wave drag as well as the induced drag have increased as a result of the higher freestream Mach number. The drag breakdown makes it clear, however, that most of the drag increment comes from the wave drag. It is interesting to note that except for the increase in induced drag due to the increase in lift, virtually no Mach-number effect on the induced drag is calculated for this configuration.

Concluding Remarks

A technique for the evaluating of aerodynamic drag from flowfield solutions based on the Euler equations is discussed. The drag-evaluation technique is limited to steady attached subsonic and transonic flows about three-dimensional configurations in the absence of surface heating/cooling and active systems such as surface blowing/suction and propulsion. The technique allows the decomposition of the total inviscid drag into drag due to vortex shedding (induced drag) and drag due to shocks (wave drag). The former component is obtained by evaluating the distribution of the trailing vorticity downstream of the trailing edge of the configuration, and the latter component of the drag is obtained by integrating the entropy rise across the shocks.

The drag-evaluation technique is applied to several three-dimensional flowfield solutions. These flowfield solutions are obtained with three quite different Euler codes at both subsonic and transonic flow conditions. The present force prediction technique is shown to work well for all three Euler codes. For all test cases the lift based on the evaluation of the trailing vorticity is shown to be in good agreement with the lift based on the integration of surface pressures. This provides a check on the consistency of the numerical solution as well as the drag prediction. The wake-evaluation technique is shown to be more consistent and accurate when it comes to the prediction of induced drag. This, together with the separate wave-drag prediction, allows the aerodynamic designer to gather detailed information on the sources of inviscid drag, thereby enhancing the efficiency of the design process for a particular configuration.

Acknowledgments

This research was sponsored by the NASA Ames Research Center under Joint Research Interchanges NCA2-397 and NCA2-581. The efforts of P. M. H. W. Vijgen were supported by Langley Research Center under Contract NAS1-18240. We also thank S. Obayashi, J. L. Thomas, and V. N. Vatsa for making available their respective Euler codes.

References

[1]Lock, R. C., "The Prediction of the Drag of Aerofoils and Wings at High Subsonic Speeds," *Aeronautical Journal*, Vol. 90, No. 896, 1986, pp. 207–226.

[2]Yu, N. J., Chen, H. C., Samant, S. S., and Rubbert, P. E., "Inviscid Drag Calculations for Transonic Flows," AIAA Paper 83-1928, July 1983.

[3]Slooff, J. W., "Computational Drag Analyses and Minimization; Mission Impossible?," *Aircraft Drag Prediction and Reduction*, AGARD-R-723, Addendum I, 1986.

[4]Van Dam, C. P., Nikfetrat, K., Chang, I. C., and Vijgen, P. M. H. W., "Drag Calculations of Wings Using Euler Methods," AIAA Paper 91-0338, Jan. 1991.

[5]Van Dam, C. P., and Nikfetrat, K., "Accurate Prediction of Drag Using Euler Methods," *Journal of Aircraft*, Vol. 29, No. 3, 1992, pp. 516–519.

[6]Oswatitsch, K., "Der Luftwiderstand als Integral des Entropiestromes," *Nachrichten der Akademie der Wissenschaften in Göttingen, Mathematisch-Physikalische Klasse*, Heft 1, 1945, pp. 88–90.

[7]Whitham, G. B., "The Flow Pattern of a Supersonic Projectile," *Communications on Pure and Applied Mathematics*, Vol. 5, 1952, pp. 301–348.

[8]Lighthill, M. J., "Higher Approximations," *General Theory of High Speed Aerodynamics*, edited by W. R. Sears, Princeton Univ. Press, Princeton, NJ, 1954, pp. 345–489.

[9]Van der Vooren, J., and Slooff, J. W., "CFD-Based Drag Prediction; State-of-the-Art, Theory, Prospects," National Aerospace Lab., NLR TP 90247 L, Aug. 1990.

[10]Weston, R. P., "Refinement of a Method for Determining the Induced and Profile Drag of a Finite Wing from Detailed Wake Measurements," Ph.D. Dissertation, Univ. of Florida, Gainesville, FL, 1981.

[11]Jameson, A., Schmidt, W., and Turkel, E., "Numerical Solution of the Euler Equations by Finite Volume Methods Using Runge Kutta Time Stepping Schemes," AIAA Paper 81-1259, June 1981.

[12]Vatsa, V. N., "Accurate Numerical Solutions for Transonic Viscous Flow over Finite Wings," *Journal of Aircraft*, Vol. 24, No. 6, 1987, pp. 377–385.

[13]Obayashi, S., Fujii, K., and Gavali, S., "Navier-Stokes Simulation of Wind-Tunnel Flow Using LU-ADI Factorization Algorithm," NASA TM 100042, Feb. 1988.

[14]Obayashi, S., Matsushima, K., and Fujii, K., "Improvements in Efficiency and Reliability for Navier-Stokes Computations Using the LU-ADI Factorization Algorithm," AIAA Paper 86-0338, Jan. 1986.

[15]Anderson, W. K., Thomas, J. L., and Van Leer, B., "Comparison of Finite-Volume Flux Splittings for the Euler Equations," *AIAA*

Journal, Vol. 24, No. 9, 1986, pp. 1453–1460.

[16]Anderson, W. K., Thomas, J. L., and Whitfield, D. L., "Multigrid Acceleration of the Flux-Split Euler Equations," AIAA Paper 86-0274, Jan. 1986.

[17]Van Dam, C. P., Nikfetrat, K., Vijgen, P. M. H. W., and Fremaux, C. M., "Calculation and Measurement of Induced Drag at Low Speeds," Society of Automotive Engineers Paper 901935, Oct. 1990.

[18]Schmitt, V., and Charpin, F., "Pressure Distributions on the ONERA-M6-Wing at Transonic Mach Numbers," *Experimental Data Base for Computer Program Assessment*, AGARD-AR-138, May 1979, pp. B1-1–B1-44.

[19]Sacher, P., "Numerical Solutions for Three-Dimensional Cases-Swept Wings," *Test Cases for Inviscid Flow Field Methods*, AGARD-AR-211, May 1985, pp. 7-1–7-110.

[20]Nikfetrat, K., Van Dam, C. P., Vijgen, P. M. H. W., and Chang, I. C., "Prediction of Drag at Subsonic and Transonic Speeds Using Euler Methods," AIAA Paper 92-0169, Jan. 1992.